ARTICLE

Electrospun Carbon Nanofibers as Low-Cost Counter Electrode for Dye-Sensitized Solar Cells

Prakash Joshi,[†] Lifeng Zhang,[‡] Qiliang Chen,[†] David Galipeau,[†] Hao Fong,*[,‡] and Qiquan Qiao*[,†]

Center for Advanced Photovoltaics, Department of Electrical Engineering, South Dakota State University, 020 EECS, Brookings, South Dakota 57007, and Department of Chemistry, South Dakota School of Mines and Technology, 501 East Saint Joseph Street, Rapid City, South Dakota 57701

ABSTRACT Electrospun carbon nanofibers (ECNs) have been explored as an electrocatalyst and low-cost alternative to platinum (Pt) for triiodide reduction in dye-sensitized solar cells (DSCs). The results of electrochemical impedance spectroscopy (EIS) and cyclic voltammetry measurements indicated that the ECN counter electrodes exhibited low charge-transfer resistance (R_{ct}), large capacitance (C), and fast reaction rates for triiodide reduction. Although the efficiency (η) of ECN-based cells was slightly lower than that of Pt-based cells, their short circuit current density (J_{sc}) and open circuit voltage (V_{oc}) were comparable. The ECN-based cells achieved an energy conversion efficiency (η) of 5.5 % under the AM 1.5 illumination at 100 mW cm^{-2}. The reason for lower cell performance using the ECN electrode was because of its lower fill factor (FF) than that of Pt-based cells, probably caused by high total series resistance (R_{Stot}) at ~15.5 Ω cm^2, which was larger than that of ~4.8 Ω cm^2 in the Pt-based devices. Simulated results showed that the fill factor (FF) and η could be substantially improved by decreasing R_{Stot}, which might be achieved by using thinner and highly porous ECNs to reduce the thickness of the ECNs counter electrode.

KEYWORDS: electrospinning • carbon nanofibers • dye-sensitized solar cells • counter electrode

INTRODUCTION

Dye-sensitized solar cells (DSCs) have attracted extensive attention as a low-cost alternative to Si solar cells (1−7). A typical DSC consists of a photoanode and a counter electrode separated by an electrolyte containing an iodide/triiodide (I^-/I_3^-) redox couple. The photoanode is usually a transparent conducting oxide (TCO) coated with a film of TiO_2 nanoparticles, while the counter electrode is a TCO coated with a thin layer of platinum (8). When dye molecules adsorbed onto TiO_2 surface are exposed to sunlight, photoelectrons are generated and injected into the photoanode; subsequently, the electrons move to the counter electrode through an external circuit. The oxidized dye molecules regain electrons from I^- ions, resulting in the oxidation of I^- ions into I_3^- ions; and the I_3^- ions are reduced into I^- ions by obtaining electrons from the counter electrode. Pt counter electrodes have been widely used in DSCs, because Pt is an efficient electrocatalyst for reduction of I_3^- ions (9−11). Nonetheless, Pt is an expensive metal and the corrosive I^-/I_3^- redox couple can reduce its catalytic activity, which raises concerns about the long-term stability of DSCs (12).

Previous studies have revealed that carbonaceous materials including graphite, carbon black, carbon nanotubes, and poly(3,4-ethylenedioxythiophene) (PEDOT) doped with *p*-toluenesulfonate (PEDOT-TsO) or polystyrenesulfonate (PEDOT-PSS), can exhibit comparable electrocatalytic performance to Pt for the reduction of I_3^- ions (3, 12−25). It is noteworthy that carbonaceous materials are abundant and low-cost and also possess high resistivity against corrosion (22). Therefore, the replacement of Pt with low-cost carbonaceous materials could facilitate the commercialization of DSCs (16−18, 26).

Herein, we report for the first time that electrospun carbon nanofibers (ECNs) can be used as a low-cost alternative to Pt counter electrodes in DSCs. The ECN-based DSCs had similar performance as that of Pt-based devices in terms of short circuit current density (J_{sc}) and open circuit voltage (V_{oc}). Electrochemical measurements indicated that the ECN counter electrode exhibited low charge-transfer resistance (R_{ct}), large capacitance (C), and fast reaction rates for I_3^- reduction, indicating that the ECN electrode is an efficient electrocatalyst for the application in DSCs.

EXPERIMENTAL SECTION

Preparation of Electrospun Carbon Nanofibers (ECN). The ECNs were developed through electrospinning of polyacrylonitrile (PAN) nanofibers, followed by thermal treatments of stabilization and carbonization (27). Prior to electrospinning, the PAN (S.A.F 3K, Courtaulds, U.K.) was first dissolved in *N*,*N*-dimethylformamide (DMF) to prepare a 14 wt. % solution. Subsequently, the solution was filled in a 30 mL BD Luer-Lok tip plastic syringe having a stainless-steel needle with 18 gauge

* To whom correspondence should be addressed. Tel.: 605-688-6965 (Q.Q); 605-394-1229 (H.F.). Fax: 605-688-4401 (Q.Q); 605-394-1232 (H.F.) E-mail: Qiquan.Qiquan@sdstate.edu (Q.Q); Hao.Fong@sdsmt.edu (H.F.).
Received for review August 16, 2010 and accepted October 26, 2010
[†] South Dakota State University.
[‡] South Dakota School of Mines and Technology.
DOI: 10.1021/am100742s

Published on Web 11/12/2010

90° blunt end. The electrospinning setup included a high voltage power supply (model number ES30P), purchased from the Gamma High Voltage Research, Inc. (Ormond Beach, FL), and a laboratory-produced roller with a diameter of 10 inches. During electrospinning, a positive high voltage of 25 kV was applied to the needle, and a flow rate of 1.0 ml/h was maintained using a digitally controlled syringe pump (model number: KDS 200) purchased from the KD Scientific Inc. (Holliston, MA). The PAN nanofibers were collected as the randomly overlaid mat on the electrically grounded aluminum foil that covered the roller. The rotational speed of the roller during electrospinning was set at 100 rpm. The collected PAN nanofiber mat had a width of ~10 cm, a thickness of ~40 μm, and a mass per unit area of ~15 g/m^2. The electrospun PAN nanofiber mat could be easily peeled from the aluminum foil after being immersed in distilled water. The thermal treatments (i.e., stabilization and carbonization) were conducted in a Lindberg 54453 Heavy Duty Tube Furnace purchased from the TPS Co. (Watertown, WI). During the stabilization, a constant flow of air was maintained through the furnace; the PAN nanofiber mat was sandwiched between two ceramic plates and heated to 280 °C at a heating rate of 1 °C/min, and the temperature was then held at 280 °C for 6 h. The stabilized nanofiber mat was subsequently heated at a rate of 5 °C/min to 1200 °C in argon followed by holding the temperature at 1200 °C for 1 h to prepare the ECN sheets. The structures of electrospun carbon nanofibers were analyzed using a Renishaw RM2000 Raman spectrometer; an argon laser beam with the wavelength of 514.5 nm was used, the spot diameter was set at 5 μm, and the detector integration time was set at 30 s.

Preparation and Characterization of the ECN Counter Electrodes. To fabricate the counter electrodes of DSCs, the ECN paste was first prepared by mixing 0.1 g of ECNs with 19.6 g of polyoxyethylene (12) tridecyl ether (POETE), following a similar method reported by Mei and Ouyang (28). To uniformly disperse the ECNs in POETE, the mixture was grinded in a mortar, sonicated, and then centrifuged at a spin speed of 10 000 rpm. The excess POETE that appeared on top of the mixture during centrifuging was removed using a pipette. The remaining mixture was then doctor-bladed onto the fluorine doped tin dioxide substrate (FTO, with a resistance and thickness of ~8 Ω/□ and ~400 nm, respectively) to make the counter electrode. The ECN counter electrode was then sintered at 200 °C for 15 min and then at 475 °C for 10 min. Electrochemical impedance spectroscopy (EIS) measurements were carried out using an Ametek VERSASTAT3-200 Potentiostat with the frequency analysis module (FDA). The AC signal had amplitude of 10 mV in the frequency range from 0.1 to 10^5 Hz at zero DC bias in the dark. Cyclic voltammetry (CV) measurements were performed using a Pt wire as counter electrode, an Ag/AgCl as reference electrode, and an ECN or Pt coated FTO as working electrode in an acetonitrile solution containing 10 mM LiI and 0.5 mM I_2 using 0.1 M tetra-*n*-butylammonium tetrafluoroborate as the supporting electrolyte at a potential scan rate of 50 mV · s^{-1}.

Device Fabrication and Characterization. For the fabrication of DSCs, the TiO_2 photoanode comprising a $TiCl_4$-treated nanocrystalline TiO_2 layer (Solaronix Ti-Nanoxide HT/SP) and a light scattering layer (Dyesol WER4-0) was prepared on a FTO glass substrate coated with a TiO_2 blocking layer. The sintered photoanode was immerged in a solution containing 0.5 mM Ruthenizer 535-bisTBA dye (Solaronix N-719) in acetonitrile/valeronitrile (1:1) for 12 h. The photoanode was then assembled with the ECN counter electrode using a thermoplastic sealant. The I^-/I_3^- electrolyte was injected into the cells. To compare the DSC performance, the devices using a sputtered Pt layer (40 nm) as counter electrode were also fabricated following the same method. The devices were tested under the AM 1.5 illumination at 100 mW cm^{-2}.

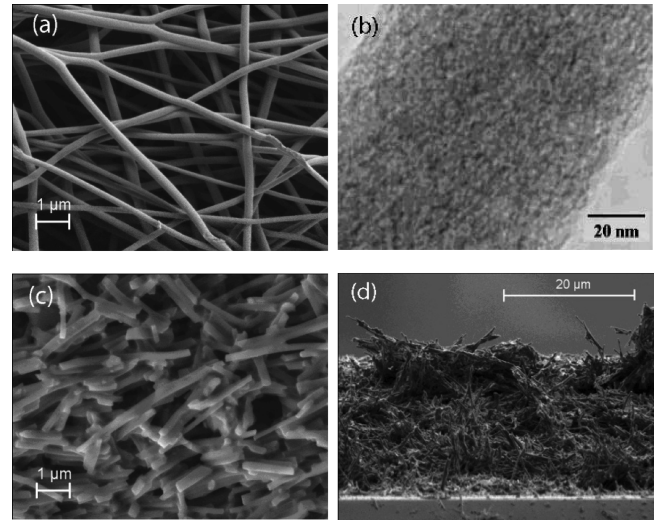

FIGURE 1. (a) Top view SEM image of the electrospun carbon nanofiber (ECN) sheets. (b) TEM image of a single typical ECN. SEM image of (c) top-view and (d) cross-section of ECN counter electrode deposited by doctor blading on a FTO-glass substrate.

RESULTS AND DISCUSSION

Figure 1 shows scanning electron microscope (SEM) and transmission electron microscope (TEM) images of the original electrospun carbon nanofibers (ECNs) and prepared ECN counter electrode deposited by doctor blading on a FTO-glass substrate. The ECNs were relatively uniform with small variations in diameter, and an average diameter of approximately 250 nm (Figure 1a). In addition, the nanofiber sheet contained no microscopically identifiable beads or beaded-nanofibers. The BET surface area of the ECN sheet was about 100 m^2/g, determined by a Micromeritics ASAP 2010 surface area analyzer using N_2 adsorption at 77 K. Because of the weak attachment of original ECN sheet onto FTO substrate, we converted the ECN sheet into a paste by adding the POETE binder, followed by grinding and sonication. When processed into a paste to make the counter electrode, the nanofibers, which were originally tens of micrometers long, were broken into submicrometers to micrometers (Figure 1c) by sonication before being deposited as counter electrode onto the FTO. The originally prepared ECN (Figure 1a) has a conductivity of ~1538 Sm^{-1} but was decreased to ~164 Sm^{-1} after processed into a paste Figure 1c. A possible reason was that the ECNs were broken into shorter sizes and the conductivity network might be reduced. In addition, the binder POETE was added and then burned away, which might leave voids between the broken ECNs. However comparing Figure 1a with Figure 1c, it can be seen that the surface area of the ECN paste made by sonication should be higher than of the original ECN sheet. The cross-section SEM image of the ECN film in Figure 1d shows that the counter electrode has a thickness of about 24 μm. This thickness seems to be higher than that of the widely studied carbon nanoparticle counter electrodes. Murakami et al. studied the carbon nanoparticle thickness effects on the DSC parameters including short circuit current density (J_{sc}), open circuit voltage (V_{oc}), fill factor (FF), and cell efficiency (η) (21). Their results show that the thickness of the carbon nanoparticle counter electrodes mainly affects

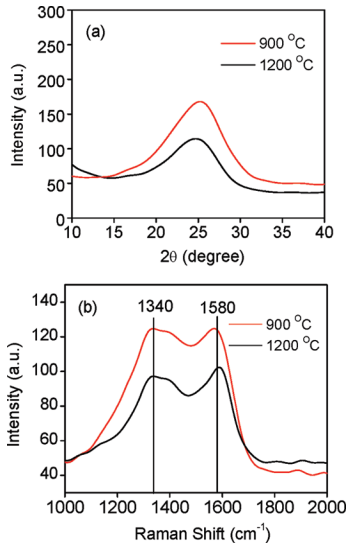

FIGURE 2. (a) X-ray diffraction (XRD) and (b) Raman spectra of ECNs with the carbonization temperatures set at 900 °C (red) and 1200 °C (black).

the FF and an optimal thickness was observed at ~14.5 μm. In our previous study on carbon nanoparticle counter electrode, the carbon nanoparticle counter electrode thickness was ~11.2 μm (20). In addition, Ramasamy et al. prepared a carbon nanoparticle counter electrode with a thickness of ~20 μm (22). The thickness of ECN counter electrode was higher than that of the carbon nanoparticle counter electrode. Figure 1c shows that the broken nanofibers were loosely packed with large spaces among them, possibly leading to a smaller surface area than that of carbon nanoparticle counter electrode. In an earlier study of the TiO_2 nanoparticle/nanofiber composite, we compared the surface area and dye attachment in the pure TiO_2 nanoparticle photoanode with that of the pure TiO_2 nanofiber photoanode (29). The TiO_2 nanofiber photoanode was also prepared similarly by making a paste using sonication. We found that the dye attachment in pure TiO_2 nanofiber photoanode was reduced by ~75% compared to pure TiO_2 nanoparticle photoanode at the same thickness, suggesting a much lower surface area in the former. Therefore, the surface area in the ECN counter electrode might also be smaller than that in carbon nanoparticle counter electrode and thus a higher thickness was used to make the ECN-based counter electrode to increase the surface area.

The TEM image in Figure 1b shows that the structure of ECNs was primarily turbostratic instead of graphitic, that is, tiny graphite crystallites with sizes of a few nanometers were embedded in amorphous carbonaceous matrix. This was further confirmed by the results acquired from X-ray diffraction (XRD) analyses as shown in Figure 2a. The diffraction peaks centered at the 2θ angles of ~25° were attributed to the crystallographic plane of (002) in graphitic structure (30, 31). The average interplanar spacing, $d_{(002)}$, was calculated to be approximately 0.355 nm. Since the $d_{(002)}$ value for naturally occurring graphite crystals is 0.335 nm (30), the graphite crystallites in the ECNs are likely less ordered. Additionally, the average size parameter, L_c, of graphite crystallites in the ECNs could arguably be determined using

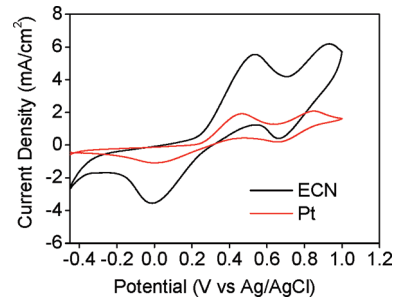

FIGURE 3. Cyclic voltammograms of the ECN (black) and Pt (red) counter electrode in an acetonitrile solution containing 10 mM LiI and 0.5 mM I_2 using 0.1M tetra-*n*-butylammonium tetrafluoroborate as the supporting electrolyte. The ratio of I^- and I_2 is 20. The reference electrode is Ag/AgCl. The thickness of the ECN and Pt counter electrode is about 24 μm and 40 nm, respectively.

the Scherrer equation (30, 31), and the value of L_c was approximately 1.1 nm.

Raman spectroscopy is a useful tool for investigating the microstructure of carbonaceous materials (32−34). The Raman spectra of carbonaceous materials have two characteristic bands including (1) "D-band", which is centered at the wavenumber of ~1340 cm^{-1} and is related to disordered and/or turbostratic carbonaceous components, and (2) "G-band", which is centered at the wavenumber of ~1580 cm^{-1} and is related to the ordered graphitic structures; that is, the G-band is attributed to the E_{2g2} C=C stretching vibrations of graphite crystallites (34), and this band is correlated to the (002) diffraction peak in the XRD curve. The positions of these two bands are irrelevant to the carbonization temperature, while the intensity ratio of the D-band to the G-band (known as the *R*-value) indicates the amount of structurally ordered graphite crystallites in the carbonaceous materials (34). The Raman spectra of ECNs with the carbonization temperatures set at 900 and 1200 °C are shown in Figure 2b. The *R*-values of the ECNs carbonized at 900 °C and 1200 °C were 1.00 and 0.95, respectively. It was evident that the *R*-value of ECNs decreased with an increase in the carbonization temperature, indicating that some disordered carbonaceous components were converted into the ordered graphite crystallites at a higher carbonization temperature.

In a previous report, Kay et al. used a mixture of graphite and carbon black as counter electrode to replace Pt and they found that the graphite, if aligned in the counter electrode plane, could increase the electrical conductivity (12). Herein, we used the ECNs carbonized at 1200 °C, which might increase the graphite content and electrical conductivity, to make the counter electrode for the DSCs. Figure 3 shows the cyclic voltammograms of the ECN and Pt counter electrode carried out in an acetonitrile solution containing 10 mM LiI and 0.5 mM I_2 using 0.1 M tetra-*n*-butylammonium tetrafluoroborate as the supporting electrolyte. The ECN counter electrodes show two pairs of oxidation and reduction peaks similar to those in the Pt electrodes. The oxidation and reduction pair on the left was attributed to the redox reaction of $I_3^- + 2e^- = 3I^-$, while that on the right resulted from the redox reaction of $3I_2 + 2e^- = 2I_3^-$ (35, 36). The right pair of oxidation and reduction of the ECN counter

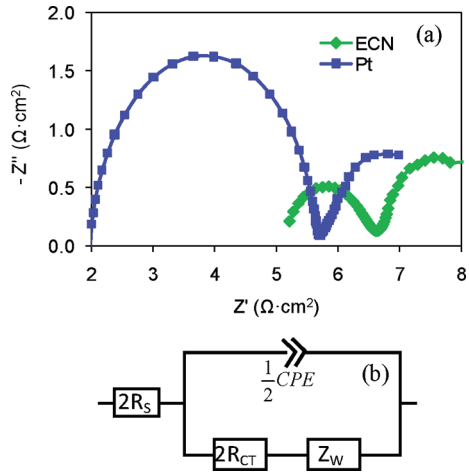

FIGURE 4. (a) Nyquist plots of a symmetrical ECN−ECN electrode or Pt−Pt electrode cell by assembling two identical ECN electrodes or platinum electrodes on each side separated by a spacer filled with electrolyte; (b) equivalent circuit of the symmetrical ECN-ECN electrode or Pt−Pt electrode electrochemical cell for EIS measurement. R_s: Series resistance at the counter electrode. CPE: Constant phase element. R_{ct}: Charge-transfer resistance. Z_w: Nernst diffusion impedance.

electrodes had a larger oxidation current density, but a smaller reduction current density than those of the Pt electrodes. This pair was from the reaction of $3I_2 + 2e^- = 2I_3^-$ and had little effect on the DSC performance (37). The left pair of peaks of the ECN counter electrodes had both a larger oxidation and reduction current density than those of the Pt electrodes. This pair was from the reaction of $I_3^- + 2e^- = 3I^-$ and directly affects the DSC performance, suggesting a fast rate of triiodide reduction. This indicates that ECNs can be used as an efficient electrocatalyst counter electrode in DSCs.

Electrochemical impedance spectroscopy (EIS) is generally used to study the catalytic performance of counter electrode (38, 39). To eliminate the TiO_2 photoanode effect, the symmetrical ECN−ECN and Pt−Pt electrochemical cells were used for EIS characterization, which were made by assembling two identical ECN (or Pt) electrodes on each side separated by a spacer containing an electrolyte of I^-/I_3^- redox couple. Figure 4a shows the Nyquist plots of the symmetrical ECN−ECN and Pt−Pt electrochemical cells. The equivalent circuit diagram used to fit the impedance spectra is shown in Figure 4b. The circuit elements consist of charge transfer resistance (R_{ct}) at the ECN-based or Pt-based electrode/electrolyte interface, series resistance (R_s), constant phase element (CPE), and Warburg impedance (Z_W) (21). The high-frequency semicircle resulted from the charge transfer process at the electrode/electrolyte interface, while the low-frequency arc was attributed to the Nernst diffusion impedance (Z_W) of the I^-/I_3^- redox couple in a thin layer of electrolyte (37, 40−42). The Nyquist plots were fitted and the results are shown in Table 1. The charge transfer resistance (R_{ct}) of the ECN electrode was found to be 0.7 Ω cm^2, which was less than half of that (1.9 Ω cm^2) of the Pt electrode, indicating a high electrocatalytic performance. The CPE represents the capacitance at the interface between

Table 1. Fitted Parameters Extracted from the Nyquist Plots of the Respective ECN and Pt Counter Electrode

counter electrode	R_s (Ω cm2)	R_{ct} (Ω cm^2)	C (F cm^{-2})	β
ECN	5.12	0.70	5.6×10^5	0.82
Pt	2.00	1.89	2.0×10^5	0.95

the ECN-based or Pt-based electrode and the electrolyte. The CPE can be depicted as

$$Z_{CPE} = \frac{1}{Y_0}(j\omega)^{-\beta}$$

where Y_0 is the CPE parameter, β is the CPE exponent ($0 < \beta < 1$), and ω is the angular frequency. Both Y_0 and β are independent of frequency.

An ideal capacitance has an exact semicircle with a β value of 1. However, several factors including surface roughness, porous films, leaky capacitor, and non-uniform current distribution can lead to a non-ideal capacitance at the interface of counter electrode and electrolyte, causing the semicircle to depress into an ellipse in the Nyquist plots (21, 39). This typically causes the β value to decrease below 1. The fitted results show that β of the ECN counter electrode was 0.82, which was smaller than the β value of 0.95 exhibited by the Pt electrode. The lower β value suggested that the ECN counter electrode had a higher porosity than the Pt catalyst (21). This is consistent with previous work in which the low β value of 0.81 was reported in a highly porous carbon nanoparticle counter electrode (21). In addition, it was found that the ECN electrode had larger capacitance (C) than the Pt electrode, suggesting a higher surface area in the former counter electrode. This is also in agreement with the results from other nanostructured counter electrodes with a high porosity (21, 41). However, the fitted results show that the series resistance of the ECN counter electrode was 5.12 Ω cm^2, which was about twice of that of 2 Ωcm^2 for the Pt electrode. This was probably caused by the large thickness (~24 μm) of the ECN counter electrode. Such results are consistent with previous reports that R_s increased with film thickness, where the R_s value for 19.5 μm carbon nanoparticle films was almost twice that of a typical Pt electrode (21).

Figure 5a shows the current density versus voltage ($J-V$) of the ECN- and Pt-based DSCs under AM 1.5 solar simulator illumination at 100 mW cm^{-2}. The DSC performance is summarized in Table 2. The ECN-based DSCs exhibited a J_{sc} of 12.6 mA cm^{-2}, V_{oc} of 0.76 V, and fill factor (FF) of 0.57, yielding a reasonable energy conversion efficiency (η) of 5.5 %. The corresponding parameters (J_{sc}, V_{oc}, FF, and η) of the Pt-based DSCs were 13.02 mA cm^{-2}, 0.75 V, 0.71, and 6.97 %, respectively. The V_{oc} of the ECN-based DSCs was 0.76 V, which was very close to that of 0.75 V of the Pt-based devices. The reverse saturation current (J_0) was calculated from the $J-V$ curves in Figure 5a. The J_0 of the ECN-based cells was 4.47×10^{-9} mA cm^{-2}, which was comparable to

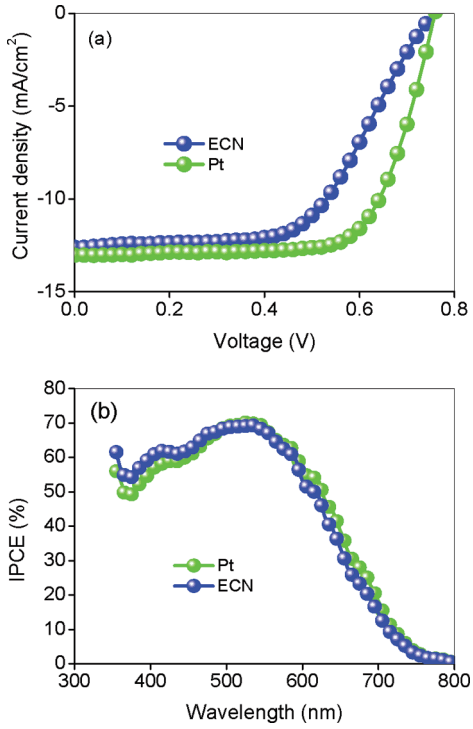

FIGURE 5. (a) Current density−voltage ($J-V$) curves and (b) incident photon-to-current conversion efficiency (IPCE) spectral action responses of the DSCs based on ECN (blue) and Pt (green) counter electrode.

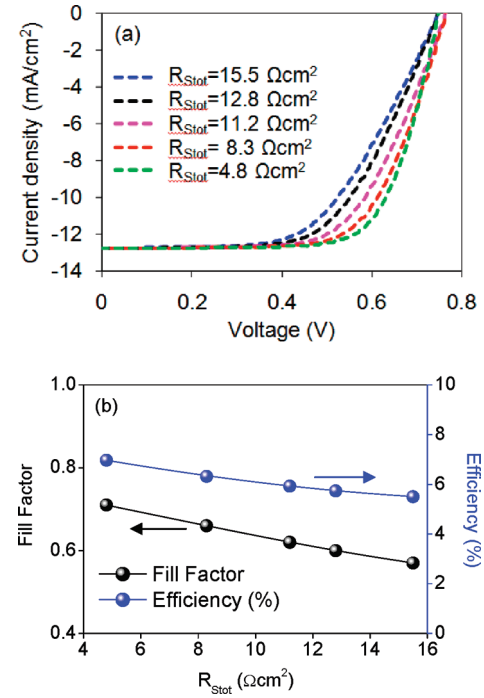

FIGURE 6. (a) Simulated $J-V$ curves of the ECN-based DSCs with various R_{Stot} including 15.5 Ω cm^2 (blue), 12.8 Ω cm^2 (dark), 11.2 Ω cm^2 (purple), 8.3 Ω cm^2 (red), 4.8 Ω cm^2 (green). (b) Dependence of FF (black) and η (blue) on R_{Stot}.

Table 2. Comparison of DSC Parameters Acquired from the ECN and Pt Counter Electrode (J_0 = Reverse Saturation Current, R_{Stot} = Total Series Resistance)

counter electrode	J_{sc} (mA cm^{-2})	V_{oc} (V)	FF	η (%)	J_0 (mA cm^{-2})	R_{Stot} (Ω cm^2)
ECN	12.60	0.76	0.57	5.5	4.47×10^{-9}	15.5
Pt	13.02	0.75	0.71	6.97	3.58×10^{-9}	4.8

that of 3.58×10^{-9} mA cm^{-2} for the Pt-based cells. Since J_0 is typically regarded as a measure of recombination in the device, this indicates that the ECN-based cells had a comparable recombination as that of the Pt-based devices. Previous studies have shown that charge recombination in DSCs at the FTO/TiO_2 and TiO_2/electrolyte interface can cause a loss in V_{oc} (43−45). The observation that the ECN based DSCs had a V_{oc} similar to that of the Pt-based devices further confirmed that the ECN counter electrodes do not affect recombination in the DSCs even at a large counter electrode thickness of ∼24 μm.

However, the ECN-based cells show a comparable but slightly lower J_{sc} than the Pt-based cells. Figure 5b shows the incident photon-to-current conversion efficiency (IPCE) spectral action responses of the ECN- and Pt-based DSCs. It was found that the IPCE of the ECN-based cells was slightly smaller than that of the Pt based devices in the 550−750 nm spectral range, which was consistent with the relatively lower J_{sc}. This was possibly attributed to unabsorbed incident light reflected back to the TiO_2 photoanode for re-absorption by the semitransparent Pt counter electrode, leading to an enhanced J_{sc} (13, 42, 46). The ECN counter electrode cannot induce such a reflection effect. However, the decrease of J_{sc} was not significant and the major reason for the relatively lower η in the ECN-based cells was the reduced FF caused by the increase of the total series resistance (R_{Stot}) of the DSC device. The R_{Stot} of the ECN-based DSCs was 15.5 Ω cm^2, which was much larger than that of 4.8 Ω cm^2 in the Pt-based devices. The increase of R_{Stot} in the ECN-based cells was probably attributed to two factors. The first factor is that the thickness of the ECN counter electrode (∼24 μm) was much thicker than the 40 nm of the Pt electrode. Although the thickness significantly increased the surface area for triiodide reduction and reduced R_{ct} at the counter electrode, it also increased the average electron transport length before reaching the site for triiodide reduction and the internal series resistance (21). The increased internal series resistance was confirmed by the R_s value of 5.12 Ω cm^2 observed in the ECN-based symmetrical cells, which was more than twice of that of 2 Ω cm^2 in the Pt-based symmetrical cells acquired from the EIS measurements. This is consistent with previous studies of carbon nanoparticle counter electrodes which indicated that series resistance increased with film thickness, resulting in a low FF and reduced η (15, 20, 22). The second factor is that the ECN counter electrode may have a higher Nernst diffusion impedance (Z_W) of the triiodide ions than the Pt electrode, which can also lead to a larger internal series resistance (13). The higher Z_W was attributed to the enhanced average diffusion length of the triiodide ions due to the large thickness of ECN electrode. Previous studies of other nanostructured counter electrodes including surface-nitrided nickel (41), carbon nanotubes (13, 40), and carbon nanoparticles (21) have also reported a higher Z_W than the Pt electrode. To quantitatively study the R_{Stot} effect on the performance of ECN-based DSCs, a

series of $J-V$ curves with different R_{Stot} were simulated (Figure 6a). The dependence of FF and η on R_{Stot} in the ECN-based DSCs is shown in Figure 6b. It is evident that the FF significantly improved with a decrease in R_{Stot} from 15.5 to 4.8 Ω cm^2, thereby leading to an increase of η. A possible approach to decreasing R_{Stot} is to reduce the thickness of the ECN counter electrode using thinner and porous carbon nanofiber sheets.

In conclusion, ECNs have been successfully demonstrated as an efficient electrocatalyst with low charge-transfer resistance (R_{ct}), large surface area, and fast reaction rates for reduction of I_3^- ions. Although the η of ECN-based cells was lower than that of Pt-based cells, their J_{sc} and V_{oc} were comparable, and the ECN based cells also exhibited a reasonable η at 5.5 % under the AM 1.5 illumination at 100 mW cm^{-2}. The R_{Stot} of the ECN based DSCs was 15.5 Ω cm^2, which was larger than that of 4.8 Ω cm^2 in the Pt-based devices; this is the major reason for the relatively lower performance of the ECN-based cells. Simulated results showed that the FF and η can be significantly improved with the decrease of R_{Stot}, which may be achieved by using thinner and highly porous ECNs to reduce the thickness of ECNs counter electrodes.

Acknowledgment. This research was partially supported by NSF CAREER (ECCS-0950731), NASA EPSCoR (NNX09-AP67A), and South Dakota NSF EPSCoR/PANS program. The authors are grateful to Dr. Mahdi F. Baroughi in the Department of Electrical Engineering and Computer Science at the South Dakota State University for help in setting up the $J-V$ and IPCE measurement systems.

REFERENCES AND NOTES

(1) Oregan, B.; Gratzel, M. *Nature* **1991**, *353*, 737–740.
(2) Gajjela, S. R.; Ananthanarayanan, K.; Yap, C.; Gratzel, M.; Balaya, P. *Energy Environ. Sci.* **2010**, *3*, 838–845.
(3) Fan, B. H.; Mei, X. G.; Sun, K.; Ouyang, J. Y. *Appl. Phys. Lett.* **2008**, 93.
(4) Yum, J. H.; Baranoff, E.; Hardin, B. E.; Hoke, E. T.; McGehee, M. D.; Nuesch, F.; Gratzel, M.; Nazeeruddin, M. K. *Energy Environ. Sci.* **2010**, *3*, 434–437.
(5) Alibabaei, L.; Wang, M. K.; Giovannetti, R.; Teuscher, J.; Di Censo, D.; Moser, J. E.; Comte, P.; Pucciarelli, F.; Zakeeruddin, S. M.; Gratzel, M. *Energy Environ. Sci.* **2010**, *3*, 956–961.
(6) Abbotto, A.; Manfredi, N.; Marinzi, C.; De Angelis, F.; Mosconi, E.; Yum, J. H.; Zhang, X. X.; Nazeeruddin, M. K.; Gratzel, M. *Energy Environ. Sci.* **2009**, *2*, 1094–1101.
(7) Zhang, G. L.; Bai, Y.; Li, R. Z.; Shi, D.; Wenger, S.; Zakeeruddin, S. M.; Gratzel, M.; Wang, P. *Energy Environ. Sci.* **2009**, *2*, 92–95.
(8) Xie, Y.; Joshi, P.; Ropp, M.; Galipeau, D.; Zhang, L. F.; Fong, H.; You, Y. J.; Qiao, Q. Q. *J. Porphyrins Phthalocyanines* **2009**, *13*, 903–909.
(9) Sun, K.; Fan, B. H.; Ouyang, J. Y. *J. Phys. Chem. C* **2010**, *114*, 4237–4244.
(10) Gratzel, M. *J. Photochem. Photobiol. C: Photochem. Rev.* **2003**, *4*, 145–153.
(11) Xie, Y.; Joshi, P.; Darling, S. B.; Chen, Q.; Zhang, T.; Galipeau, D.; Qiao, Q. *J. Phys. Chem. C* **2010**, *114*, 17880–17888.
(12) Kay, A.; Gratzel, M. *Sol. Energy Mater. Sol. Cells* **1996**, *44*, 99–117.
(13) Lee, W. J.; Ramasamy, E.; Lee, D. Y.; Song, J. S. *ACS Appl. Mater. Interfaces* **2009**, *1*, 1145–1149.
(14) Imoto, K.; Suzuki, M.; Takahashi, K.; Yamaguchi, T.; Komura, T.; Nakamura, J.; Murata, K. *Electrochemistry* **2003**, *71*, 944–946.
(15) Imoto, K.; Takahashi, K.; Yamaguchi, T.; Komura, T.; Nakamura, J.; Murata, K. *Sol. Energy Mater. Sol. Cells* **2003**, *79*, 459–469.
(16) Burnside, S.; Winkel, S.; Brooks, K.; Shklover, V.; Gratzel, M.; Hinsch, A.; Kinderman, R.; Bradbury, C.; Hagfeldt, A.; Pettersson, H. *J. Mater. Sci.—Mater. Electron.* **2000**, *11*, 355–362.
(17) Hinsch, A.; Behrens, S.; Berginc, M.; Bonnemann, H.; Brandt, H.; Drewitz, A.; Einsele, F.; Fassler, D.; Gerhard, D.; Gores, H.; Haag, R.; Herzig, T.; Himmler, S.; Khelashvili, G.; Koch, D.; Nazmutdinova, G.; Opara-Krasovec, U.; Putyra, P.; Rau, U.; Sastrawan, R.; Schauer, T.; Schreiner, C.; Sensfuss, S.; Siegers, C.; Skupien, K.; Wachter, P.; Walter, J.; Wasserscheid, P.; Wurfel, U.; Zistler, M. *Prog. Photovolt: Res. Appl.* **2008**, *16*, 489–501.
(18) Skupien, K.; Putyra, P.; Walter, J.; Kozlowski, R. H.; Khelashvili, G.; Hinsch, A.; Wurfel, U. *Prog. Photovolt: Res. Appl.* **2009**, *17*, 67–73.
(19) Suzuki, K.; Yamaguchi, M.; Kumagai, M.; Yanagida, S. *Chem. Lett.* **2003**, *32*, 28–29.
(20) Joshi, P.; Xie, Y.; Ropp, M.; Galipeau, D.; Bailey, S.; Qiao, Q. *Energy Environ. Sci.* **2009**, *2*, 426–429.
(21) Murakami, T. N.; Ito, S.; Wang, Q.; Nazeeruddin, M. K.; Bessho, T.; Cesar, I.; Liska, P.; Humphry-Baker, R.; Comte, P.; Pechy, P.; Gratzel, M. *J. Electrochem. Soc.* **2006**, *153*, A2255–A2261.
(22) Ramasamy, E.; Lee, W. J.; Lee, D. Y.; Song, J. S. *Appl. Phys. Lett.* **2007**, *90*, 173103.
(23) Calandra, P.; Calogero, G.; Sinopoli, A.; Gucciardi, P. G. *Int. J. Photoenergy.* **2010**, *2010*, 109495.
(24) Saito, Y.; Kitamura, T.; Wada, Y.; Yanagida, S. *Chem. Lett.* **2002**, 1060–1061.
(25) Saito, Y.; Kubo, W.; Kitamura, T.; Wada, Y.; Yanagida, S. *J. Photochem. Photobiol. A* **2004**, *164*, 153–157.
(26) Han, H. W.; Bach, U.; Cheng, Y. B.; Caruso, R. A.; MacRae, C. *Appl. Phys. Lett.* **2009**, *94*.
(27) Mukherjee, K.; Teng, T. H.; Jose, R.; Ramakrishna, S. *Appl. Phys. Lett.* **2009**, *95*, 012101.
(28) Mei, X.; Ouyang, J. *Carbon* **2009**, *48*, 293–299.
(29) Joshi, P.; Zhang, L.; Davoux, D.; Zhu, Z.; Galipeau, D.; Fong, H.; Qiao, Q. *Energy Environ. Sci.* **2010**, *3*, 1507–1510.
(30) Zussman, E.; Chen, X.; Ding, W.; Calabri, L.; Dikin, D. A.; Quintana, J. P.; Ruoff, R. S. *Carbon* **2005**, *43*, 2175–2185.
(31) Iwashita, N.; Park, C. R.; Fujimoto, H.; Shiraishi, M.; Inagaki, M. *Carbon* **2004**, *42*, 701–714.
(32) Mittal, J.; Bahl, O. P.; Mathur, R. B. *Carbon* **1997**, *35*, 1196–1197.
(33) Endo, M.; Kim, C.; Karaki, T.; Kasai, T.; Matthews, M. J.; Brown, S. D. M.; Dresselhaus, M. S.; Tamaki, T.; Nishimura, Y. *Carbon* **1998**, *36*, 1633–1641.
(34) Jawhari, T.; Roid, A.; Casado, J. *Carbon* **1995**, *33*, 1561–1565.
(35) Sun, H.; Luo, Y.; Zhang, Y.; Li, D.; Yu, Z.; Li, K.; Meng, Q. *J. Phys. Chem. C* , *114*, 11673–11679.
(36) Huang, Z.; Liu, X.; Li, K.; Li, D.; Luo, Y.; Li, H.; Song, W.; Chen, L.; Meng, Q. *Electrochem. Commun.* **2007**, *9*, 596–598.
(37) Xiaoguang, M.; et al. *Nanotechnology* **2010**, *21*, 395202.
(38) Papageorgiou, N.; Maier, W. F.; Gratzel, M. *J. Electrochem. Soc.* **1997**, *144*, 876–884.
(39) Hauch, A.; Georg, A. *Electrochim. Acta* **2001**, *46*, 3457–3466.
(40) Li, G.-R.; Wang, F.; Jiang, Q.-W.; Gao, X.-P.; Shen, P.-W. *Angew. Chem. Int. Ed.* **2010**, *49*, 3653–3656.
(41) Jiang, Q. W.; Li, G. R.; Liu, S.; Gao, X. P. *J. Phys. Chem. C* **2010**, *114*, 13397–13401.
(42) Wang, M.; Anghel, A. M.; Marsan, B. t.; Cevey Ha, N.-L.; Pootrakulchote, N.; Zakeeruddin, S. M.; Graltzel, M. *J. Am. Chem. Soc.* **2009**, *131*, 15976–15977.
(43) Huang, S. Y.; Schlichthorl, G.; Nozik, A. J.; Gratzel, M.; Frank, A. J. *J. Phys. Chem. B* **1997**, *101*, 2576–2582.
(44) Gratzel, M. *Prog. Photovolt: Res. Appl.* **2000**, *8*, 171–185.
(45) Xia, J.; Masaki, N.; Jiang, K.; Yanagida, S. *J. Phys. Chem. C* **2007**, *111*, 8092–8097.
(46) Fang, X. M.; Ma, T. L.; Guan, G. Q.; Akiyama, M.; Kida, T.; Abe, E. *J. Electroanal. Chem.* **2004**, *570*, 257–263.

AM100742S